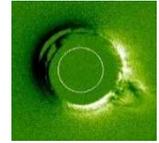# Analysis of a Type II Solar Radio Burst Observed on 20 October 2017

Whitham D. Reeve

1. Introduction

A Type II solar radio burst was observed on 20 October 2017 near the end of the UTC day at Cohoe Radio Observatory in Alaska in circular polarization and at UNAM – Instituto de Geofísica unidad Michoacan in Mexico in linear polarization. Both stations are part of the e-Callisto solar radio spectrometer network {eCallisto}. The received burst was observed to have fundamental, harmonic and split-band characteristics in the frequency range 45 to 85 MHz. Measurements of the burst may be used to infer the speed of the associated coronal mass ejection (CME) and the coronal magnetic field.

In the following sections, I provide a general description of the production, propagation and characteristics of the Type II radio burst (section 2) followed by a brief description of the overall solar event that produced the radio burst observed on 20 October (section 3). Next, the burst is analyzed for its frequency characteristics, estimated CME shock speed, estimated magnetic field in the radio burst area and other parameters (section 4). I primarily use graphical analysis. The methods demonstrate how radio data and spacecraft imagery can be used for comparison and to gain a more complete knowledge of the CME associated with a Type II radio burst. Finally, the results are discussed (section 5). For most quantities and constants I use SI units with the exception of some distances and magnetic flux densities.
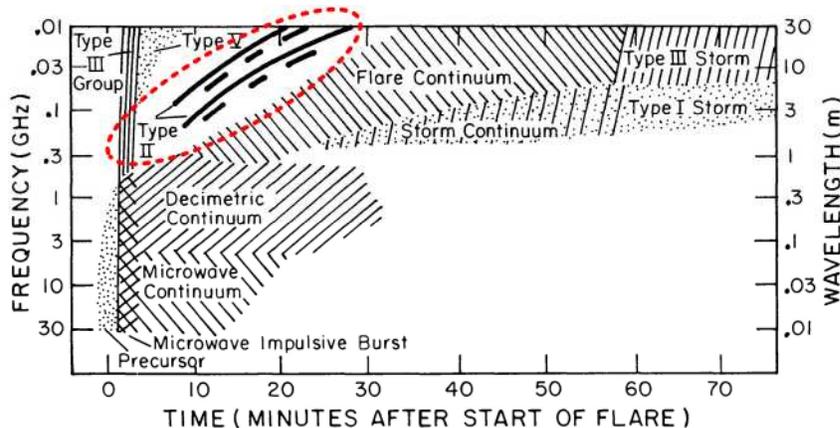

Figure 1 ~ Dynamic spectra of solar radio bursts that might be produced by a strong flare. Burst types have been categorized as Types I through V. Individual solar events will vary greatly – some burst types may be weak or missing. Of interest in this paper are Type II bursts outlined in red. Source: Figure 11 in [Dulk]

It is quite clear from the literature that there is no universal understanding or agreement on the processes that produce Type II radio bursts. The rather simple ideas and analyses put forth in this paper are based on commonly accepted methods and meant as a starting place for my own future investigations. I was inspired to do these analyses by [Monstein12]. Other works are cited where used and are listed in section 6. A good general reference for solar radio astronomy is [Kundu].

2. Characteristics and Productions of Type II Solar Radio Bursts

The Type II radio emission, or burst, is one of five general types of radio emissions generated by the Sun (figure 1). Type II solar radio emissions occur with very energetic eruptions in the Sun's atmosphere and typically indicate a coronal mass ejection is associated with a flare event. In general, Type II emissions are preceded by a few to several minutes by an intense solar flare, which is thought to be caused by instabilities in the Sun's magnetic field, and followed by a coronal mass ejection (CME), which is detected in solar imagery tens of minutes later. If the CME is Earth-directed, it may cause a geomagnetic disturbance a day or week later. The flare produces a blast wave and mass acceleration and is the initiating agent for the radio burst. Type II radio bursts have fairly narrow directional characteristics and are more likely to be received on Earth when the radio source region (typically above a flare site) is near the central meridian.

General characteristics of Type II radio bursts: A Type II radio burst is characterized by relatively slow frequency drift in both the fundamental and harmonic frequencies. Drift rates up to 1 MHz s^{-1} have been reported but rates on the order of 100 to 200 kHz s^{-1} are much more common. Type II radio bursts typically last from 3 to 30 min and are relatively rare compared to the much more common Type III fast drift radio bursts. Type II bursts (and other solar radio activity) follow the solar sunspot cycle with fewer occurrences in the years surrounding sunspot minimum.

The fundamental frequencies of the Type II burst usually fall below 150 MHz, roughly corresponding to solar altitudes in the lower corona (figure 2). The 2nd harmonic usually is near a 2:1 ratio but propagation conditions in the solar corona can significantly reduce that ratio. Generally, the 2nd harmonic has higher intensity than the fundamental (figure 3). Band-splitting is often associated with Type II bursts in which the fundamental and harmonic seen in the dynamic spectra are each split into two distinct spectral regions.
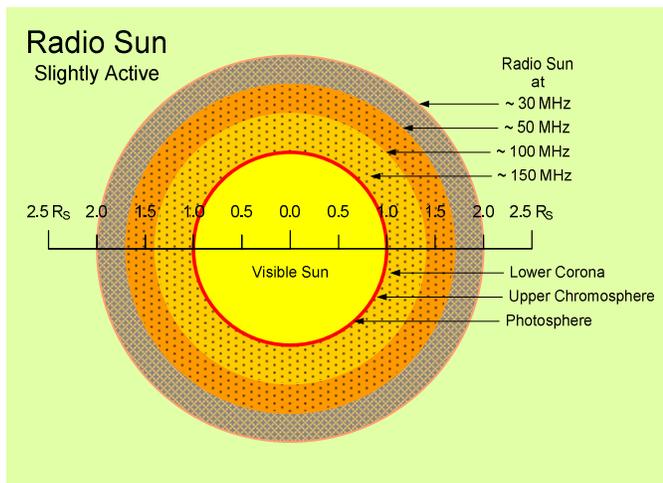

Figure 2 ~ Conceptual radio Sun, showing very roughly the distances from the center of the Sun in multiples of the visible Sun radius R_S for the characteristic plasma frequencies indicated by concentric shells. The photosphere, chromosphere and lower corona regions are indicated by callouts. The frequencies shown are based on the Newkirk corona density model for slightly active Sun discussed later. The heliocentric distance for a given frequency varies with the solar cycle and related activity, and the actual radio Sun is wider at the equator than at the poles.

Terrestrial observatories have detected Type II bursts at VHF (*meter* wavelengths) and down to the ionospheric cutoff in the HF range of about 10 to 15 MHz (*decameter* wavelengths) but spacecraft have detected them as low as 30 kHz (*kilometer* wavelengths). Generally, the lower frequencies are produced in a coronal region farther from the Sun's photosphere than higher frequencies. Type II bursts may be weakly polarized but most are unpolarized (random polarization).
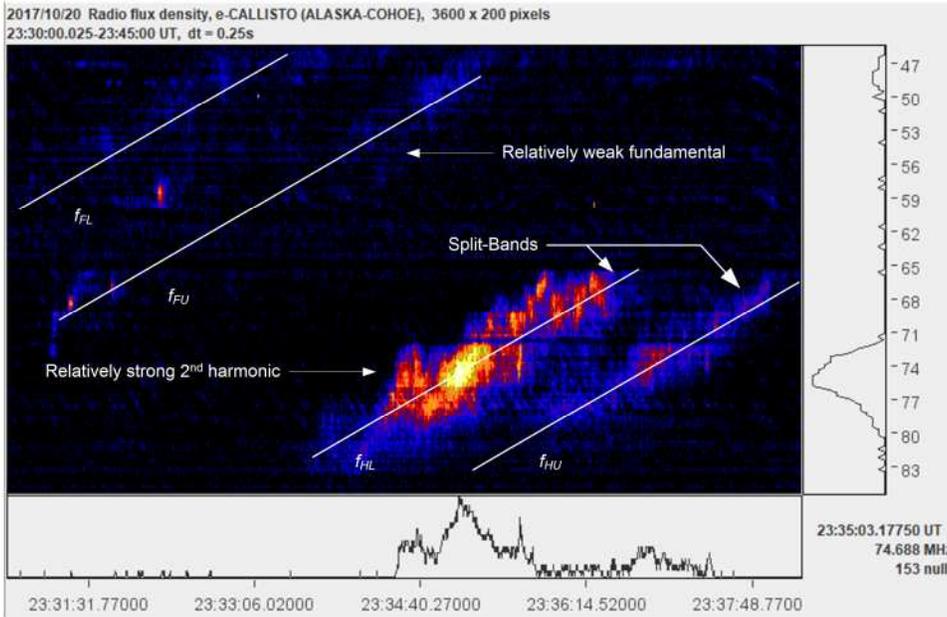
Figure 3 ~ Annotated spectrogram showing the general characteristics of a Type II radio burst with fundamental, 2nd harmonic and band-splitting characteristics. Frequency is shown along the right vertical axis with the lowest frequency at the top. Time is shown along the bottom horizontal axis and increases to the right. In this burst, the fundamental is above and to the left and the 2nd harmonic is below and to the right. The bands are indicated by straight lines marked f_{FU} and f_{FL} for fundamental upper and lower and f_{HU} and f_{HL} for harmonic upper and lower.

A possible scenario: The CME is a magnetohydrodynamic (MHD) shock wave moving through the coronal plasma (figure 4). The plasma is a conducting medium consisting of electrons and ions immersed in the Sun's magnetic field. On a large scale, the plasma has an overall neutral charge. The MHD shock causes turbulence in the corona, leading to oscillations in the electrons, which are much less massive than the ions. Instabilities in the electron gas produces fundamental and 2nd harmonic electromagnetic radiation close to the local electron plasma frequencies. A single emission mechanism does not explain current observational data.
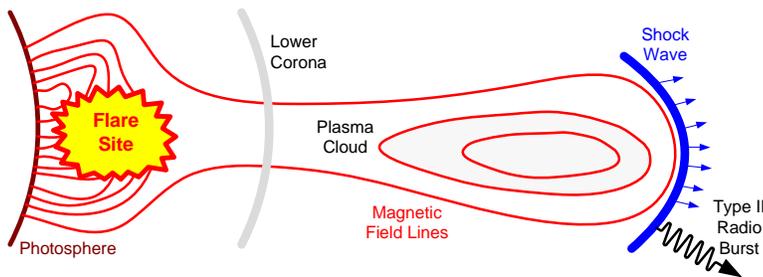

Figure 4 ~ A plasma cloud is blown away from the Sun's surface (photosphere) by an intense flare resulting in a magnetohydrodynamic shock wave and a Type II solar radio burst. Not all flares produce a Type II burst but, generally, the stronger the flare the more likely a Type II radio burst will be produced. Magnetic field lines are shown in red and the shock wave in blue.

As the shock moves outward through the corona and encounters progressively lower electron densities, the frequencies decrease thus accounting for the Type II radio sweep from higher to lower frequencies. The plasma frequency is given by (for example, see [Choudhuri])

$$f_P = \sqrt{\frac{N_e \cdot e^2}{4 \cdot \pi^2 \cdot \varepsilon_0 \cdot m_e}} \text{ Hz}$$

(1)

where

N_e electron density, m^{-3}
e electron charge, $1.60 \cdot 10^{-19}$ C
m_e electron mass, $9.11 \cdot 10^{-31}$ kg
ε_0 permittivity of free space, $8.85 \cdot 10^{-12}$ m^{-3} kg^{-1} s^4 A^2

Based on these constants, equation (1) reduces to

$$f_P = \sqrt{\frac{N_e \cdot e^2}{4 \cdot \pi^2 \cdot \varepsilon_0 \cdot m_e}} = \sqrt{\frac{N_e \cdot (1.60 \cdot 10^{-19})^2}{4 \cdot \pi^2 \cdot (8.85 \cdot 10^{-12}) \cdot (9.11 \cdot 10^{-31})}} = 8.98 \cdot \sqrt{N_e} \text{ Hz} \qquad (2)$$

Units check: $f_P = \sqrt{\dfrac{N_e \cdot e^2}{4 \cdot \pi^2 \cdot \varepsilon_0 \cdot m_e}} = \sqrt{\dfrac{m^{-3} \cdot (C)^2}{(m^{-3} kg^{-1} s^4 A^2) \cdot (kg)}} = \sqrt{\dfrac{m^{-3} A^2 s^2}{m^{-3} kg^{-1} s^4 A^2 kg}} = \sqrt{\dfrac{1}{s^2}} = s^{-1} = Hz$

Electron density in corona: Solving equation (2) for the electron density gives

$$N_e = \left(\frac{f_P}{8.98}\right)^2 \text{ m}^{-3} \qquad (3)$$

The electron density in the solar corona in terms of the distance from the Sun's center (heliocentric distance) has been modeled by a number of investigators. These models and equation (3) can be used to relate the observed frequencies during a Type II burst to the heliocentric distance. The change in frequency and thus the change in distance with respect to time then can be used to estimate the shock speed. A relatively simple and often-used density model is [Newkirk61] (figure 5), which states

$$N_e = N_0 \cdot \alpha \cdot (10^{4.32/R}) \text{ cm}^{-3} \qquad (4a)$$

$$N_e = 4.2 \cdot 10^4 \cdot \alpha \cdot (10^{4.32/R}) \text{ cm}^{-3} \qquad (4b)$$

$$N_e = 4.2 \cdot 10^4 \cdot \alpha \cdot (10^{4.32/R}) \cdot 10^6 \text{ m}^{-3} \qquad (4c)$$

where N_0 is the baseline density used by Newkirk, α is an electron density enhancement factor and R is the distance from the center of the Sun in multiples of the solar radius R_S ($6.96 \cdot 10^5$ km). The density enhancement factor is meant to account for the solar activity level (higher activity is associated with higher density) and has typical values as follows:

α = 1: Quiet Sun
α = 2: Slightly active Sun
α = 3: Moderately active Sun
α = 4: Very active Sun

Note that α does not have to be an integer. Although the overall solar activity level at the time of the burst studied here was quite low (the Sun was near the minimum of sunspot cycle 24), an active region on the Sun produced the flare and radio burst. However, there is no guidance to suggest using a low or high value of α under these circumstances. For this reason, a range of values for α is used in the later computations.
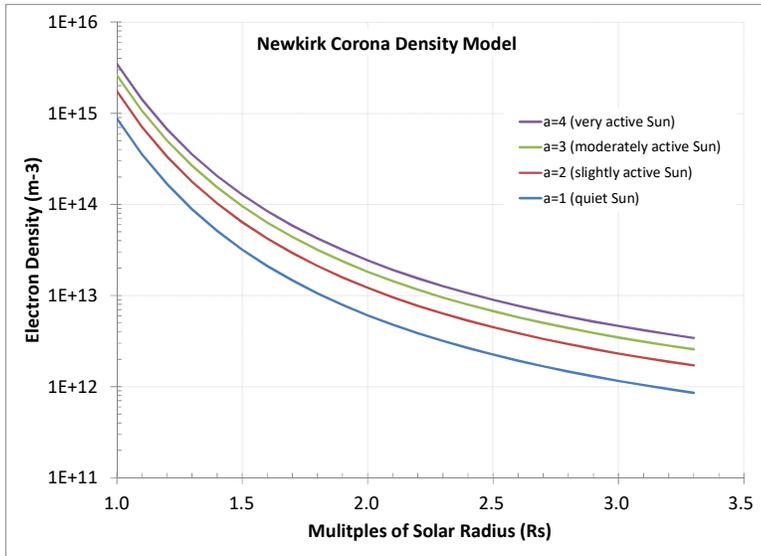
Figure 5 ~ Plot of corona electron density model based on [Newkirk61]for four solar activity levels. The densities are shown in terms of the heliocentric distance in multiples of the solar radius. To convert the density to cm^{-3}, divide by 1000 (subtract 3 from the exponent on the vertical axis).

Heliocentric distance of burst radiation: Equation (4c) can be solved for R in terms of frequency by taking the base-10 logarithm of both sides of the equation and rearranging terms, or

$$\log(N_e) = \log\left[4.2 \cdot 10^4 \cdot \alpha \cdot \left(10^{4.32/R}\right) \cdot 10^6\right] = 10.62 + log(\alpha) + \frac{4.32}{R} \tag{5}$$

$$R = \frac{4.32}{\left[\log(N_e) - 10.62 - \log(\alpha)\right]} \text{ m (for } f_p \text{ in Hz and } N_e \text{ in m}^{-3}) \tag{6a}$$

Substituting equation (3) gives

$$R = \frac{4.32}{\left[2 \cdot \log\left(\dfrac{f_p}{8.98}\right) - 10.62 - \log(\alpha)\right]} \text{ m (for } f_p \text{ in Hz and } N_e \text{ in m}^{-3}) \tag{6b}$$

Rate of change of R with respect to time: Different frequencies produced by the Type II burst occur at different times and heliocentric distances. Therefore, the average speed of the CME shock V_{Shock} between two locations can be determined from

$$V_{Shock} = \frac{\Delta R}{\Delta t} = \frac{R_{t2} - R_{t1}}{t_2 - t_1} \text{ m s}^{-1} \tag{7}$$

where

R_{t1} heliocentric distance in m at time $t1$ in s
R_{t2} heliocentric distance in m at time $t2$ in s

Summary of procedures for estimating the shock speed: As indicated above, several steps are required to estimate the shock speed from an observed Type II radio burst, in summary:
  1. Determine the frequencies at various times (usually done graphically);

2. Determine the electron densities corresponding to the frequencies using equation (3) and then determine the heliocentric distances corresponding to those densities using equation (6a);
3. Alternately, determine the heliocentric distances corresponding to the frequencies using equation (6b);
4. Determine the rate of change of distance with respect to time using equation (7) to obtain the speed.

Ambient corona magnetic field: Type II radio bursts that have band-splitting characteristics can be used to estimate the ambient magnetic field along the path of the shock propagating through the solar corona (for example, see [Smerd75]). The cited method assumes that the band-splitting occurs because of plasma emissions at different frequencies upstream and downstream of the MHD shock front as it moves through the corona. The Alfvén wave associated with the shock travels at the *Alfvén speed*. It is affected by the conditions in the Sun's atmosphere and is described by the *Alfvén Mach number*. The Alfvén Mach number is similar in concept to the Mach number used to describe the ratio of aircraft speed to the speed of sound in the Earth's atmosphere except that it applies to the Sun's atmosphere. The ratio of the shock speed to the Alfvén speed defines the Alfvén Mach number.

The spectral width of the Type II burst band splitting is related to the ratio of the downstream and upstream electron densities across the shock front, called *shock compression ratio*, and the Alfvén Mach number. Using information on the electron densities and shock speed, the magnetic field at the shock front can be estimated. It should be noted that the literature describes other methods for estimating the solar magnetic field at various heliocentric distances such as using the degree of circular polarization along with the plasma frequency [Hariharan15]. I made no attempt to use this method.

For the method I used, the variables involved in the calculations are inferred from subjective graphical measurements described later; there is considerable room for interpretation. Also, the calculated magnetic field is sensitive to the electron density, but the calculated electron density depends on the accuracy of the density model used. As noted above, I use the model described in [Newkirk61], which, in turn, uses a density enhancement factor for which no simple, useful guidance is provided. Therefore, the magnetic field calculation results presented later are given for a range of enhancement factors.

The procedures outlined below follow those given in [Cho07], which are based on [Smerd75]. The first step in determining the magnetic field is to find the *relative instantaneous bandwidth BDW* at each moment during the Type II burst given by

$$BDW = \frac{\Delta f}{f} = \frac{(f_{FU} - f_{FL})}{f_{FL}} = \frac{f_{FU}}{f_{FL}} - 1 \tag{8}$$

where f_{FU} and f_{FL} are the upper and lower bands of the split fundamental, respectively. If necessary, the 2nd harmonic band frequencies may be used after adjusting by the 2nd harmonic-to-fundamental frequency ratio. Most investigators use a 2.0 factor even though the measured ratio may be smaller; therefore,

$$BDW = \frac{(f_{HU}/2)}{(f_{HL}/2)} - 1 \tag{9}$$

where f_{HU} and f_{HL} are the upper and lower bands of the split harmonic, respectively.

Next, the shock compression ratio X (often called *density jump*) across the shock front is found from

$$X = \frac{ND_e}{NU_e} \tag{10}$$

where ND_e and NU_e are the electron densities downstream and upstream of the shock front, respectively. Equation (3) is substituted in (8) to give

$$BDW = \frac{f_{FU}}{f_{FL}} - 1 = \sqrt{\frac{ND_e}{NU_e}} - 1 \tag{11}$$

Solving for the density ratio gives

$$\frac{ND_e}{NU_e} = \left(BDW + 1\right)^2 \tag{12}$$

Substituting equation (12) in (10) gives

$$X = \left(BDW + 1\right)^2 \tag{13}$$

Assuming the shock front is perpendicular to the magnetic field, the Alfvén Mach number M_A is related to the shock compression ratio by

$$M_A = \sqrt{\frac{X \cdot (X+5)}{2 \cdot (4-X)}} \tag{14}$$

The Alfvén speed V_A is related to the shock speed V_{Shock} and Alfvén Mach number M_A by

$$V_A = \frac{V_{Shock}}{M_A} \ \text{m s}^{-1} \tag{15}$$

As a final step, the Sun's magnetic field is found using the Alfvén speed and electron density in the upstream region, which is inferred from the fundamental low band frequency f_{FL}, or

$$B_S = 5.1 \cdot 10^{-14} \cdot f_{FL} \cdot V_A \ \text{G} \tag{16}$$

Equation (16) uses Hz and m s^{-1} for frequency and speed, respectively. The constant $5.1 \cdot 10^{-14}$ is such that the resulting magnetic flux density is in *gauss* (G) units rather than the SI unit *tesla* (T) because gauss is more convenient when dealing with the Sun's magnetic field.

CME propagation: The coronal mass ejection indicated by a Type II radio burst accelerates and propagates near its shock speed away from the Sun, but the matter experiences deceleration as it blows away until reaching a near-constant speed. If the CME is Earth-directed, its arrival at Earth's magnetosphere is indicated by a pulse on terrestrial magnetometers. A geomagnetic storm may or may not follow depending on the interplanetary magnetic field associated with the CME. It is for this reason that analyses of Type II bursts are a critical element in space weather prediction. Earth is approximately 215 solar radii (1 Astronomical Unit, AU) away from the Sun, and an Earth-directed CME requires from one to nine days in transit depending on its speed along the Sun-Earth path.

3. Overall Solar Event of 20 October

The overall event is described in reports issued by NOAA's Space Weather Prediction Center (SWPC). The *Solar and Geophysical Event Report* for late in the day 20 October includes three components, an x-ray flare, radio burst at 245 MHz and radio sweep in the range 25 to 180 MHz (table 1) {EVENT}. SWPC also issued an *Alert* early the next day at 0000 specifically for the Type II radio burst {ALERT}. Alerts for Type II bursts include an estimate of the associated shock speed, which SWPC calculates for the mass ejected from the Sun's corona, in this case 344 km s^{-1}.

Because coronal mass ejections are important in space weather predictions and are generally associated with Type II radio bursts, the shock speed is an important parameter as previously explained in section 2. SWPC also reported in its *Forecast Discussio*n for 21 October: *"Solar activity reached moderate levels today after newly numbered Region 2685 (S10E78, Hsx/alpha) produced an M1 flare at 20/2328 UTC. Associated with the event was a Type II radio sweep and a CME signature observed in SOHO/LASCO C2 imagery beginning at 21/0000 UTC. Preliminary analysis suggests no Earth-directed component was present."* {FRCST} The active region is shown in SDO imagery (figure 6). The M1 flare most likely was the initiating agent for the Type II burst.

Table 1 ~ Extract from SWPC solar Events report from 20 October 2017 showing only the time period of the Type II burst discussed in this paper. The radio sweep (RSP) was reported at 2335 to 2339 UTC by the Palehua Solar Observatory (PAL) in Hawaii just after an M1.1 X-ray event (XRA) detected by GOES15 (G15) spacecraft at 2328. A weak burst (RBR) at 245 MHz was noted at 2327 by the Learmonth Observatory (LEA) in Australia. Source: ftp://ftp.swpc.noaa.gov/pub/indices/events/20171020events.txt

```
1490 +     2310   2328    2337  G15  5   XRA  1-8A      M1.1    8.8E-03   2685
1490       2327   2327    2327  LEA  G   RBR  245       110
1490 +     2335   ////    2339  PAL  C   RSP  025-180   II/1    344
```
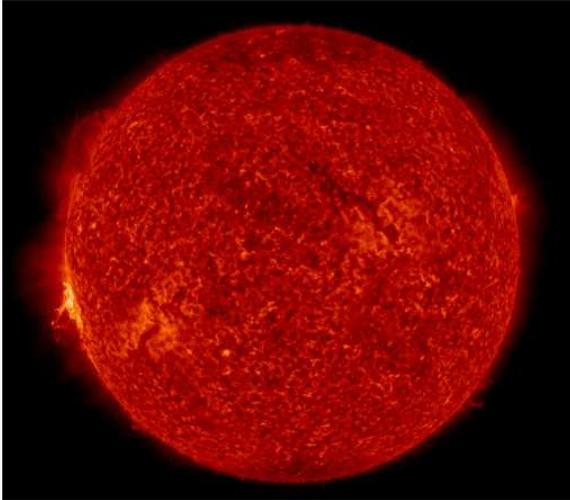
Figure 6 ~Image of the Sun at 304 Å wavelength taken at 2329 UTC on 20 October by the Solar Dynamics Observatory (SDO) very close to the time of the flare and Type II radio burst. The active region in question is numbered AR2685 and can be seen on the Sun's southeastern (lower-left) limb. The Sun was otherwise spotless at the time. Image source: {NASA}

4. Radio Observations for 20 October 2017

Stations and spectra: The Type II emission occurred near minimum of the current solar cycle (cycle 24) and was observed at two e-Callisto stations, one in Alaska USA and the other in Michoacan Mexico (table 2, figure 7). Only data from the Cohoe Radio Observatory (figure 8) is used in the following analyses. The stations produce a series of Flexible Image Transport System (FITS) data files with 15 minute lengths. Each file consists of nominal 200 frequency channels and four observations per second at each frequency (3600 x 200 pixels). These files were processed to produce the spectra used in the analyses (figure 9).

Table 2 ~ e-Callisto stations.

Station	Coordinates (°)	Elevation (m AMSL)	Frequency (MHz)	Polarization	Antenna
Cohoe Radio Observatory, Cohoe, Alaska USA	60.37N, 151.32W	22	45 to 95	Circular	LWA
UNAM, Morelia, Michoacan Mexico	19.48N, 101.41W	1970	45 to 225	Linear	LPDA

Table key: LWA: Long Wavelength Array; LPDA: Log Periodic Dipole Array; AMSL: Above Mean Sea Level
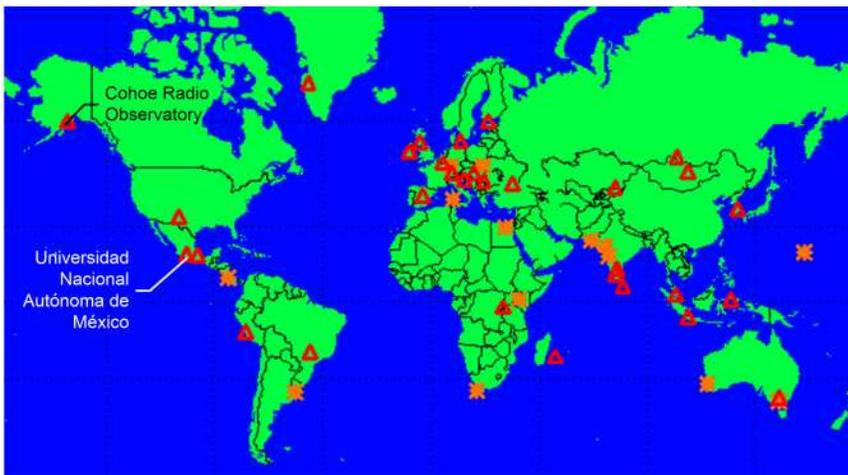

Figure 7 ~ e-Callisto Solar Radio Spectrometer Network. The two stations that observed the Type II emission on 20 October 2017 are annotated. Underlying image source: {Callisto}

Figure 8 ~ Cohoe Radio Observatory is located in southcentral Alaska on the Kenai Peninsula near the Kasilof River. At the time of the burst studied here, the Sun was 16° above the local horizon on a true azimuth of 207°. Underlying image source: USGS
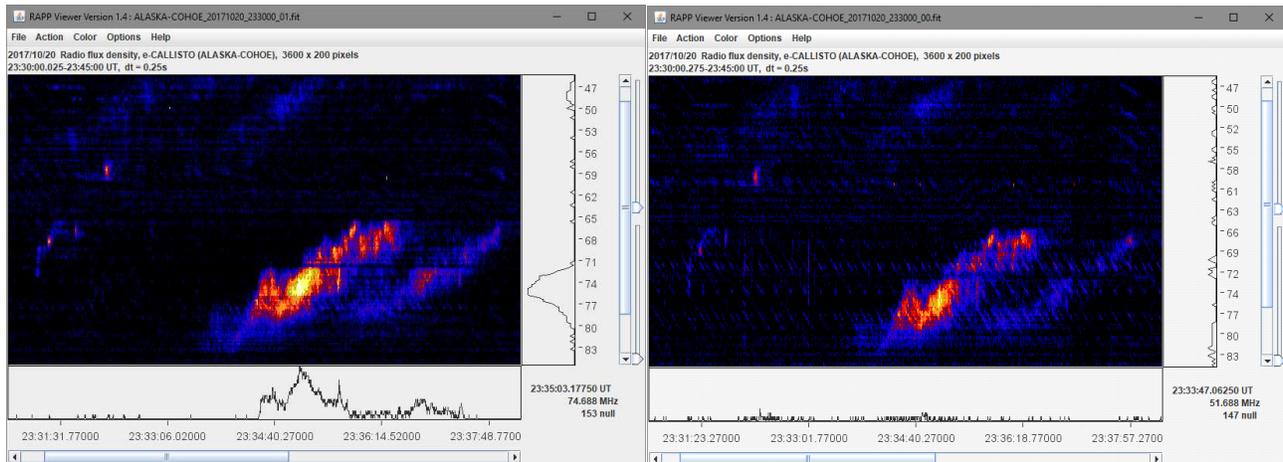

Figure 9 ~ Cohoe, Alaska USA: LHCP (left image) and RHCP (right image) circular polarizations, Bandwidth: 300 KHz, Integration time: 1 ms per pixel, LWA crossed-dipole antenna. Both polarizations have approximately the same intensity but the Left polarization is favored slightly in the 2nd harmonic, which is seen lower and to the right in the images.

Frequency drift rate and band split analyses: This and the following subsections use the data from Cohoe Radio Observatory. The instrument is setup for 200 frequency channels of which 192 are usable from 45 to 93 MHz (250 kHz channel separation). The channel sweep rate is 800 channels s^{-1}. The burst drift rate and split bands are determined from graphical analyses of the dynamic spectra (figure 10). Such a graphical analysis requires interpretation of sometimes faint spectra and thus yields subjective results.

Three methods may be used for the graphical analyses: (1) The data are first plotted using the RAPPViewer Java program {RAPPV}. The resulting display is zoomed to show only the spectra of interest. The mouse cursor is placed at spectral points of interest such as the ridges of each band, and the frequency and time values corresponding to the mouse cursor position are read from the lower-right corner of the RAPPViewer window. These values may be entered in a spreadsheet program for calculation; (2) A screenshot of the dynamic spectra is saved as a Portable Network Graphics (PNG) file. The image is then inserted in a drawing program such as the Visio application software, where lines are drawn to align with the burst. In the case of frequency drift and band-splitting, the lines are visually centered on the ridges of each band. The various distances are measured using the Visio dimension tools and scaled to time in seconds and frequency in megahertz; and (3) An interactive Python software tool (by C. Monstein) is used to display the spectrogram similar to RAPPViewer, but the values

read with the mouse cursor are automatically entered into calculations built into the tool. Methods (2) and (3) are used in the following subsections.
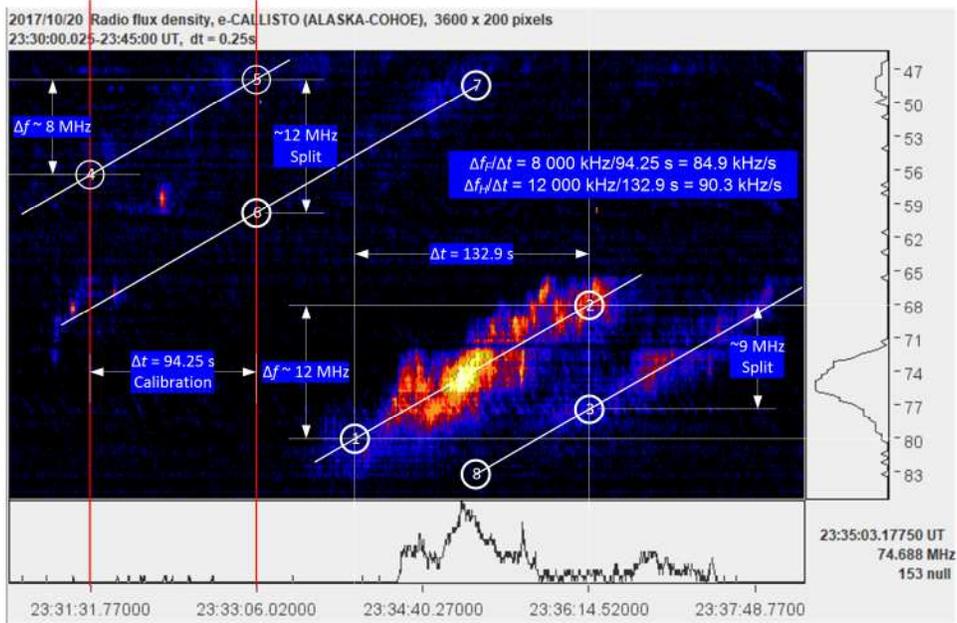

Figure 10 ~ Graphical calculations of drift rate (slope) and band split from CRO data. The vertical red lines were used to calibrate the time scale and the frequencies were estimated based on tick marks. For the fundamental $\Delta f_F/\Delta t$ = 84.9 kHz-s^{-1} (points 4 and 5) and f_{split} = 12 MHz (points 5 and 6). For the 2nd harmonic $\Delta f_H/\Delta t$ = 90.3 kHz-s^{-1} (points 1 and 2) and f_{split} = 9 MHz (points 2 and 3). The ratio of the harmonic to fundamental = 1.71 (points 7 and 8). Interpretation of the slope and middle of each band can lead to significant variations in these values.

CME shock speed: Two methods are used to determine shock speed: (1) The spectra are manually measured from the spectral plot as above; and (2) The spectra are measured using a graphical Python software tool developed specifically for the purpose.

Manual graph method: Although a good estimate can be made of the spectrogram fundamental frequencies, I have used the 2nd harmonic (figure 11) and then adjusted the measurements based on the 2nd harmonic-to-fundamental ratio. The graphical measurements are summarized (table 3).
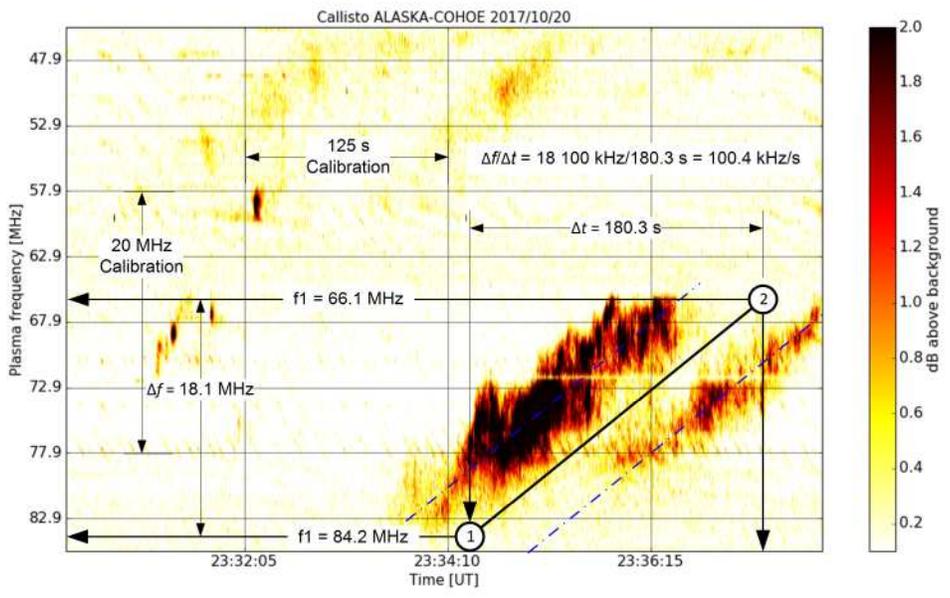

Figure 11 ~ Graphical measurements for calculating shock speed. The same CRO FITS data as above are used except that it has been plotted using a Python plot tool, which uses a different color map and background subtraction method than previous spectrograms. The 2nd harmonic is used for the measurements and then adjusted to the fundamental (see text). The solid black line between points 1 and 2 is placed midway between the two ridges of the fundamental sweep, which are marked by the thin dotted-dashed blue lines.

Table 3 ~ Results from graphical measurements of harmonic
frequencies and times

Parameter	Value	Remarks
$f1$	84.2 MHz	2nd harmonic at time 1
$f2$	66.1 MHz	2nd harmonic at time 2
Δf	18.1 MHz	
Δt	180.3 s	
$\Delta f / \Delta t$	100.4 kHz/s	

As noted, the graphical measurements of the 2nd harmonic need to be adjusted to the fundamental. It was found in the previous subsection that the ratio of the 2nd harmonic to fundamental is 1.71, and it is assumed this value applies throughout the burst frequency range. It should be noted that this ratio is about 12% lower than the average value 1.95 found statistically for a large number of Type II radio bursts (but a lower ratio does occur). With the 1.71 ratio, the fundamental frequencies used in the shock speed calculations are

For the fundamental at time 1: $f1_F = f1_H/1.71 = 84.2/1.71 = 49.2$ MHz

For the fundamental at time 2: $f2_F = f2_H/1.71 = 66.1/1.71 = 38.7$ MHz

From equation (6) with a midrange electron density enhancement factor, $\alpha = 2$

At frequency $f1$ and time t1, $R1 = \dfrac{4.32}{\left[2 \cdot \log\left(\dfrac{49.2 \cdot 10^6}{8.98}\right) - 10.62 - \log(2)\right]} = 1.69 \cdot R_s$

The distance is $R1_s = 1.69 \cdot R_s = 1.69 \cdot 6.96 \cdot 10^5 = 1.18 \cdot 10^6$ km

At frequency $f2$ and time t2, $R2 = \dfrac{4.32}{\left[2 \cdot \log\left(\dfrac{38.7 \cdot 10^6}{8.98}\right) - 10.62 - \log(2)\right]} = 1.84 \cdot R_s$

The distance is $R2_s = 1.84 \cdot R_s = 1.84 \cdot 6.96 \cdot 10^5 = 1.28 \cdot 10^6$ km

Based on these heliocentric distances and the measured time difference found in the graphical measurements (180.3 s), the shock speed calculated from equation (7)

$$V_s = \frac{\Delta R}{\Delta t} = \frac{R2_s - R1_s}{t_2 - t_1} = \frac{1.28 \cdot 10^6 - 1.18 \cdot 10^6}{180.3} = 579 \text{ km/s}$$

Similar calculations using electron density enhancement factors $\alpha = 1$ (quiet Sun) through $\alpha = 4$ (very active Sun) yield other solar radii and shock speeds (table 4). These calculations are much higher than the shock speed of 341 km/s determined by SWPC. The speed provided by SWPC may be a plane-of-sky speed (that is, based on the projected CME movement, not taking to account the direction angle), whereas the speed derived from the radio

burst is the actual radial speed. Other sources of difference may be my method of measurement and simplifications in the model as I use it here.

Table 4 ~ Estimated shock speeds and solar radii for various electron density enhancement factors and compared to the SWPC estimate

α	V_{shock} (km s^{-1})	R2	R1	Remarks
1	459	1.63	1.41	Quiet Sun
2	579	1.84	1.69	Slightly active Sun
3	673	1.99	1.81	Moderately active Sun
4	753	2.11	1.92	Very active Sun
	344	–	–	NOAA SWPC (see text)

For reference, the electron densities corresponding to the plasma frequencies used above are

$$N1_e = \left[\frac{f1}{8.98}\right]^2 = \left[\frac{49.2 \cdot 10^6}{8.98}\right]^2 = 3.0 \cdot 10^{13} \ m^{-3}$$

$$N2_e = \left[\frac{f2}{8.98}\right]^2 = \left[\frac{38.7 \cdot 10^6}{8.98}\right]^2 = 1.9 \cdot 10^{13} \ m^{-3}$$

To put these densities in perspective, the electron density in Earth's F-region ionosphere can reach about 10^{12} m^{-3}, only about one order of magnitude less than in the Sun's corona at a heliocentric distance of about 1.6 solar radii.

Software graph method: The interactive Python graphical tool (called *newkirk0.py*) uses the same FITS data files as before. The PC mouse is used to mark frequencies in the display of the Type II burst (figure 12), and the corresponding intensity-frequency-time pixels are then used in the calculations based on the Newkirk corona density model previously mentioned. It is necessary to specify an electron density enhancement factor α and integer harmonic ratio for these calculations. In the previous manual measurements I used a 2nd harmonic-to-fundamental ratio of 1.71 but for the software method I had to use the integer 2 (that value seems to be more common in the literature than a decimal fraction, anyway). For the measurements shown, the average speed is 571 km s^{-1} (shown in the lower-right of the summary plots).

As with drawing lines on a plot image described previously the mouse placement on the burst display is subjective, so this type of analysis is best done by averaging the results from a number of different measurement runs. The results from each run are averaged to obtain a final estimate (table 5). Although the results are given to one decimal place, the method is not that precise.

Table 5 ~ Average of average shock speeds using the software method with α = 1 and harmonic ratio = 2

Run	V_{shock} (km s^{-1})	Remarks
2	552.5	
3	531.4	
4	563.8	
5	525.0	
6	510.9	

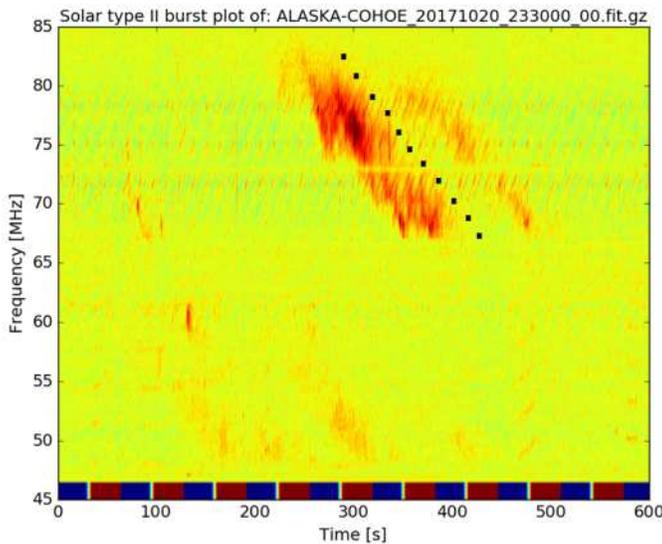Avg   536.7   Average of 5 runs

Figure 12-a ~ Graphical measurements for estimating shock speed using the newkirk0.py software tool. This tool plots frequency from low to high starting at the bottom of the left vertical scale. Time along the bottom horizontal scale is counted in seconds from an arbitrary starting point. The small black squares are selected points used in the calculations. They are placed approximately half-way between the high and low spectral ridges. The color map is set by trial-and-error and was set here for best contrast.
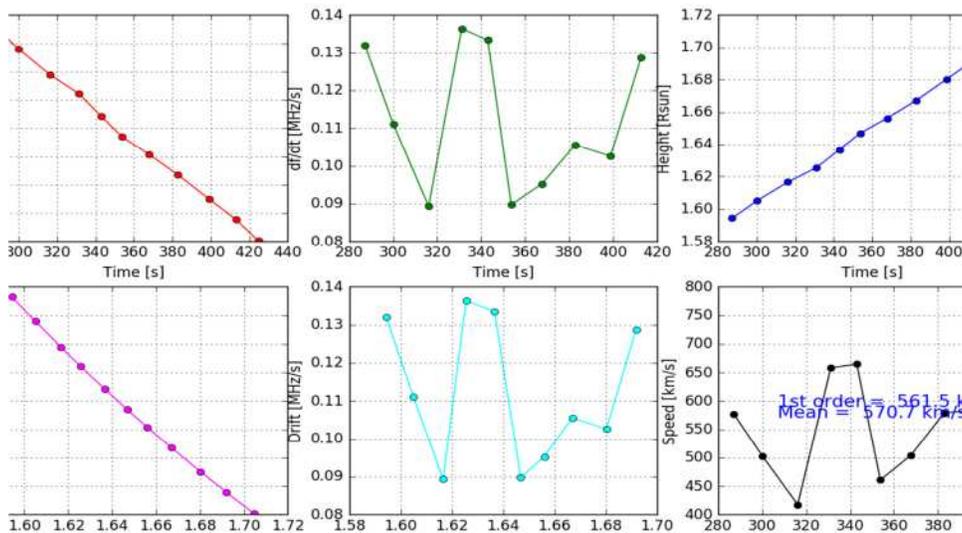

Figure 12-b ~ Summary plots of calculations using the Newkirk model with a = 1 (quiet Sun) and 2nd harmonic using a 2.0 harmonic-to-fundamental ratio. The plots show the frequency, drift rate, solar radii and CME speeds for different times based on the points selected in the spectra above. The plots are produced by the Python code and show values reasonably close to the previous manual graphical measurements and calculations. A mid-time distance is approximately 1.65 solar radii.

Comparison with other available data: Space Weather Prediction Center apparently uses a Sequential Filter Imaging Radiometer (SFIR) in the US Air Force Radio Solar Telescope Network (RSTN) to measure CME shock speeds. I have not yet accessed this data. Meanwhile, the coronagraphs on the STEREO spacecrafts provide imagery {STEREO} that may be used to estimate CME speed (figure 13). The procedures are to download and view time sequence images of the CME and calculate average speeds from equation (7) based on the graphical measurements of the shock distances and image time-stamps. I used Visio for the measurements in the same manner as previously described.

This method is somewhat crude and it has several pitfalls: (1) Due to plane-of-sky, or image projection, the measured speed may be lower than the radial speed measured from the Type II burst; (2) It may be difficult to choose the correct shock if there is more than one at a given time; (3) It is necessary to track the same shock feature – typically the leading edge – in each image, which may be difficult (as seen below); (4) A given image

wavelength may not show the needed detail so it is necessary to check other wavelengths to get a better overview; and (5) The physical scale is immense but the image dimensions are tiny, which could lead to large measurement errors.
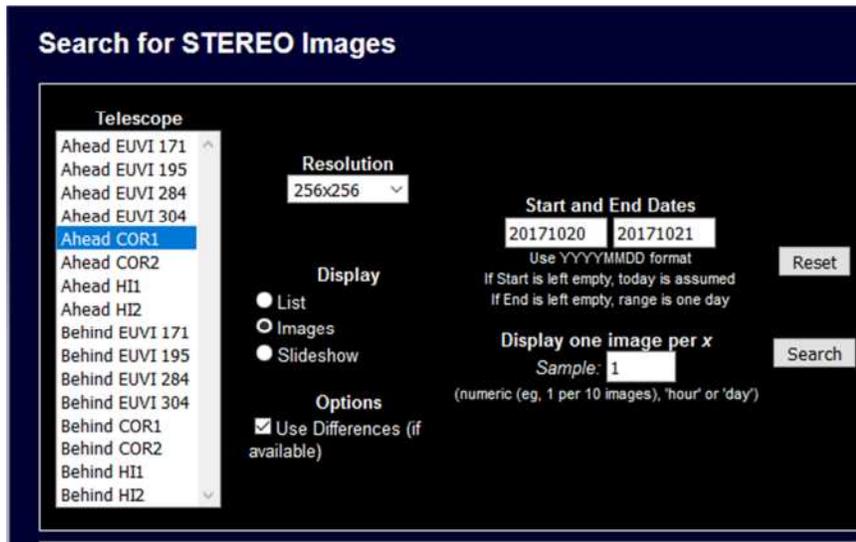

Figure 13 ~ Input window for the STEREO Science Center webpage. A wide selection of image types is available from the STEREO Ahead (A) spacecraft including coronagraph and various wavelengths. It is necessary to look at several to find the best imagery. The *Use Differences* Option can aid in tracking a feature in the shock images but difference images are not always available. Note: STEREO Behind (B) has been out of service since fall 2014. Image source: NASA

The STEREO images capture the evolution of the CME after about 1.7 solar radii while a Type II radio burst usually gives more information about later movement into interplanetary space, especially for bursts that sweep to lower frequencies (equivalent to larger heliocentric distances). Combining STEREO and Type II radio analyses allows more complete determinations of CME shock speed evolution.

Using the available imagery from STEREO (figure 14), I graphically measured the distance traveled in each successive image to determine average speeds (table 6). One example is shown for illustration (figure 15). The speeds using this method were measured at greater solar radii than the radio burst and yielded lower values in the neighborhood of 369 km s^{-1} as opposed to 459 and 537 km s^{-1} for the radio burst analyses. This might be partly explained by deceleration of the CME shock as it propagates through the Sun's corona.
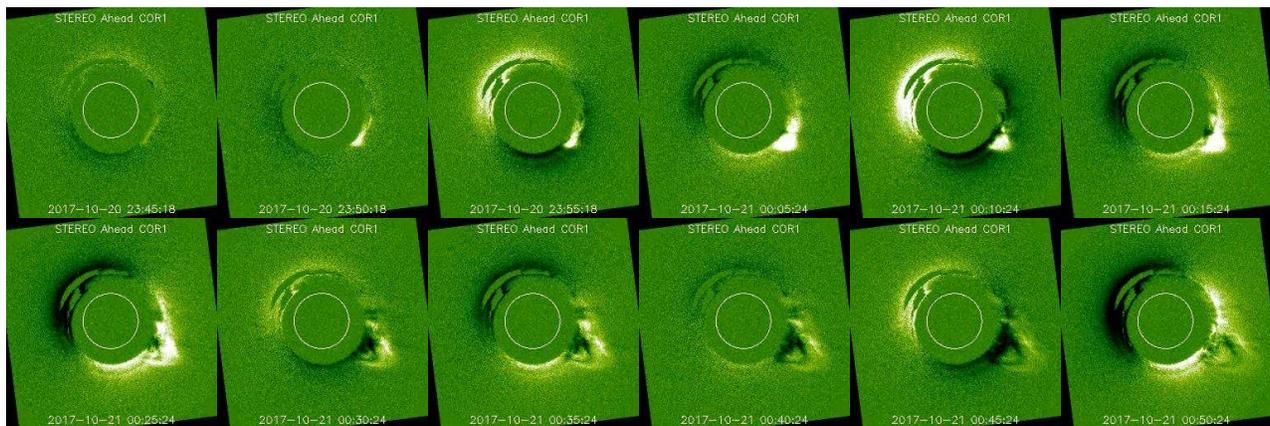

Figure 14 ~ Time series of STEREO coronagraph images at 5 min intervals starting 20 October at 23:45:18 and ending 21 October at 00:50:24 (two images are missing from the sequence). In images not shown here I could see trailing parts of the CME up to about 03:00. Left-to-right, top-to-bottom: The CME can be seen immerging in the lower-right corner of the coronagraph. The Sun is blocked by the imager occulting disk and is outlined in white. The disk is 2 solar radii in diameter

and is used for relative distance measurements. The time stamps on the images are used for relative time measurements. Each speed calculation gives the average speed between two measured points. The shock emergence in the first image is at 1.67 solar radii. The shock has reached approximately 3.74 solar radii in the last image. Images source: NASA

Table 6 ~ Average shock speeds using STEREO images in previous figure. It is difficult to see the same feature on images 7 – 12 so the distances are anomalous especially for images 7, 8 and 9. The shaded line shows the average for all images. R is given in multiples of the solar radii $R_s = 6.96 \cdot 10^5$ km.

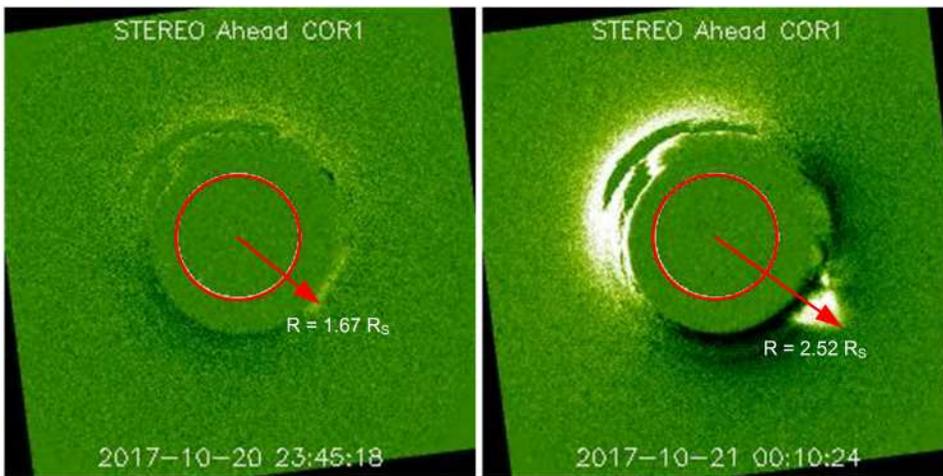| Image	ΔR	Δt (s)	V_{shock} (km s^{-1})	Image	ΔR	Δt (s)	V_{shock} (km s^{-1})
1 – 2	1.67 – 1.90 = 0.23	300	534	7 – 8	2.86 – 3.07 = 0.21	300	487
2 – 3	1.90 – 2.08 = 0.18	300	418	8 – 9	3.07 – 3.05 = -0.02	300	–
3 – 4	2.08 – 2.38 = 0.30	606	345	9 – 10	3.05 – 3.33 = 0.18	300	418
4 – 5	2.38 – 2.52 = 0.14	300	325	10 – 11	3.33 – 3.53 = 0.20	300	464
5 – 6	2.52 – 2.68 = 0.16	300	371	11 – 12	3.53 –3.74 = 0.19	300	441
6 – 7	2.68 – 2.86 = 0.18	600	209	1 – 12	1.67 – 3.74 = 2.07	3906	369

Figure 15 ~ Two STEREO images (1 and 5) separated by 25:06 minutes or 1506 s. The shock front has traveled from 1.67 to 2.52 solar radii, corresponding to a distance of 591 600 km and an average speed of 393 km s^{-1}. The occulting disk color has been changed to red for clarity. Images source: NASA

The results from the various methods for calculating shock speed described above are summarized (table 7).

Table 7 ~ Summary of CME shock speed measurements

Source	Method	V_{shock} (km s^{-1})	Remarks
Spectrogram	Manual	459	Quiet Sun
Spectrogram	Software	537	Quiet Sun
STEREO Images	Manual	369	Images 1 ~ 12
STEREO Images	Manual	393	Images 1 & 5
SWPC	-	343	

Magnetic field analysis: The magnetic field analysis follows the same basic graphical measurement procedures used for the sweep speeds previous calculated. The steps are as follows:
1. Measure a series of upper and lower band frequencies from the plot (example, figure 16);
2. In this example, the 2nd harmonic is used and the measured values are then converted to fundamental frequencies using the 2nd harmonic-to-fundamental ratio previously calculated (example, 1.71);
3. Use the fundamental frequencies f_{FU} and f_{FL} to determine the relative bandwidths BDW from equation (8);
4. Determine the shock compression ratios from equation (13) using the BDW values;

5. Calculate the Alfvén Mach numbers M_A for the shock front using equation (14);
6. Determine the Alfvén speeds V_A from equation (15) using M_A;
7. Calculate the solar magnetic field at each location from equation (16) using the lower band fundamental frequencies f_{FL} and Alfvén speeds V_A.
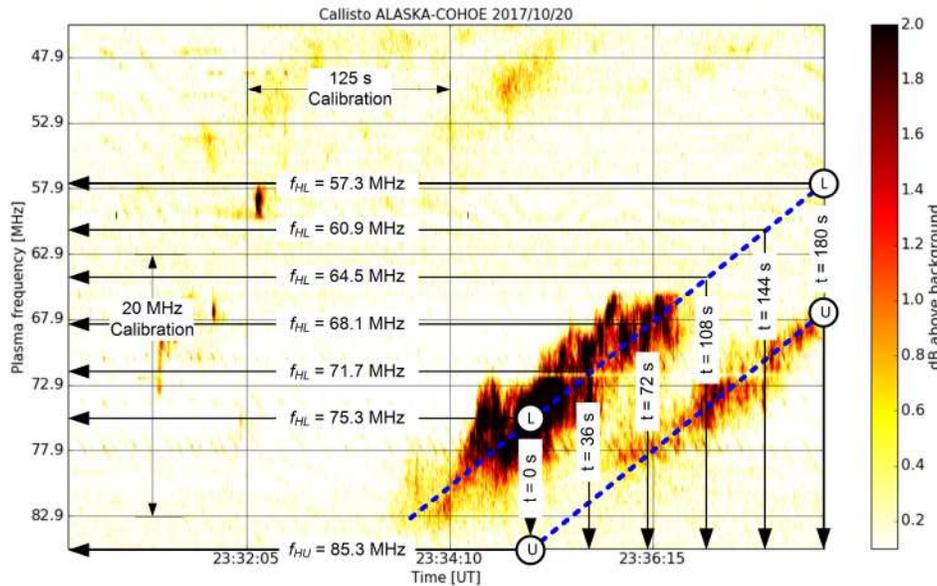

Figure 17 ~ Graphical measurements for calculating magnetic field. Lines are placed through the 2nd harmonic of the burst spectra and used to determine six values for the lower band along with corresponding times measured from t = 0 s (2335:00 UTC). The upper band is determined in the same way. The measurements cover a total time of 180 s. The straight line estimates indicate a constant 10 MHz separation between the upper and lower bands of the 2nd harmonic. It should be noted that curved (rather than straight) lines may be needed for analysis.

Table 8 ~ Estimated frequencies, times and derived parameters for magnetic field calculations. Frequencies f_{HU} and f_{HL} are graphically measured 2nd harmonics and f_{FU} and f_{FL} are derived fundamentals using the ratio 1.71. The calculated Alfvén speed V_A is based on a shock speed V_{Shock} = 459 km s^{-1} and quiet Sun, α = 1

time (s)	f_{HU} (MHz)	f_{HL} (MHz)	f_{FU} (MHz)	f_{FL} (MHz)	BDW	X	M_A	V_A (km s^{-1})
0	85.3	75.3	49.9	44.0	0.133	1.28	1.22	377
36	81.7	71.7	47.8	41.9	0.139	1.30	1.23	373
72	78.1	68.1	45.7	39.8	0.147	1.32	1.24	369
108	74.5	64.5	43.6	37.7	0.155	1.33	1.26	365
144	70.9	60.9	41.5	35.6	0.164	1.36	1.28	360
180	67.3	57.3	39.4	33.5	0.175	1.38	1.30	354

This method lends itself to easy calculation in a spreadsheet program. Estimates are summarized for the shock speed corresponding to a quiet Sun (table 8). For comparison, the calculated magnetic field is plotted for each time-stamp using four electron density enhancement factors, α =1 through α = 4, corresponding to quiet, slightly active, moderately active and very active Sun (figure 17). It is noted that the estimated magnetic field decreases as the distance from the Sun increases, which is the expected profile. The estimated coronal magnetic field calculated here is comparable to other investigations (figure 18).
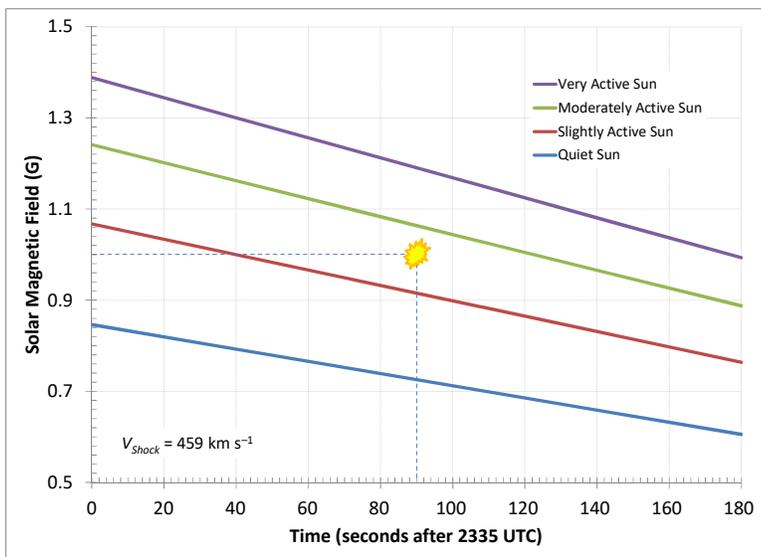
Figure 17 ~ Estimated solar magnetic field assuming various solar activity levels and constant CME shock speed V_{Shock} = 459 km s^{-1}. These estimates are based on manual graphical measurements using a straight-line approximation of upper and lower fundamental frequency bands. A mid-time average magnetic flux density based on all solar activity levels is about 0.97 G.

For comparison: Magnetic flux density on Earth's surface at the equator is about 0.3 G (or 31 000 nT).
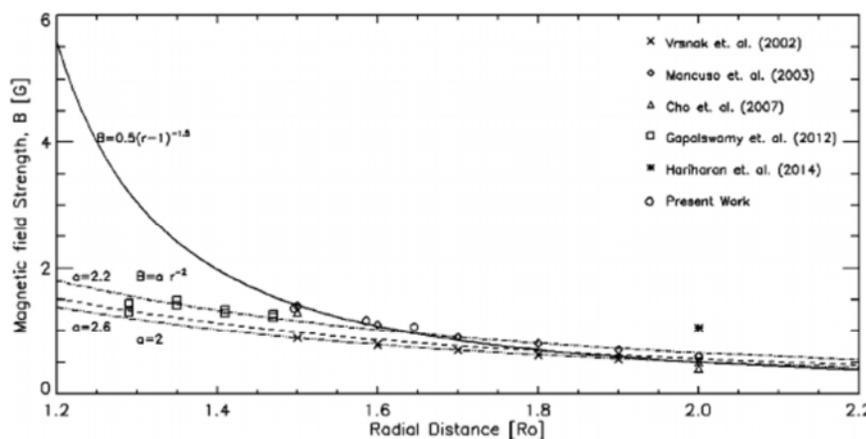

Figure 18 ~ Comparative solar magnetic field estimates by several investigators. The dashed lines are from Type II burst measurements and the solid line is from an empirical relationship. The values are closely clustered and at 1.65 solar radii are about 1 G, which agrees very well with the previous chart. Image source: Figure 6, in [Hariharan15].

Polarization analysis: Type II radio bursts generally are not polarized. Even if weakly polarized, Faraday Rotation in Earth's ionosphere could be great enough to reduce the certainty of any terrestrial polarization measurements. Also, the Sun's corona could produce significant rotation and a consequent dispersion that could depolarize the radio waves. Nevertheless, in this subsection I calculate various polarization parameters on the assumption that any received polarization is circular.

The Callisto instruments at CRO are connected to the outputs of the quadrature coupler in the LWA Power Coupler (LWAPC-Q), one for right-hand circular polarization (RHCP) and one for left-hand circular polarization (LHCP). The associated CRO data files with -00 suffix are RHCP and -01 are LHCP. The polarization characteristics can be analyzed by computing

- ✿ Total power or intensity of all the received radiation, Stokes I parameter in equation (17)
- ✿ Difference in the power of the received radiation in each polarization, a measure of the net circular polarization, Stokes V parameter in equation (18)
- ✿ Degree of circular polarization (d_{CP}) or Stokes V/I in equation (19)

Note: I have not yet obtained comparable data from a professional observatory to confirm the polarization rotation directions. Therefore, the rotation directions used in this section are subject to change, although the

computations are not affected. The polarization parameters are computed for each frequency-time pixel in the FITS data files and plotted in the figures indicated.

The Stokes I and V parameters are found from (see, for example, chapter 2 in [Marr])

$$I = LHCP + RHCP \text{ (figure 19)} \tag{17}$$

$$V = |LHCP - RHCP| \text{ (figure 20)} \tag{18}$$

The degree of polarization is found from (see, for example, chapter 4 in [Kraus])

$$d_{CP} = \frac{V}{I} = \frac{|LHCP - RHCP|}{LHCP + RHCP} \text{ (figure 21)} \tag{19}$$

The CRO data does not include any linear polarization measurements, so Stokes Q and U parameters cannot be computed.

The data indicate that total power (Stokes I) is strongest near 75 MHz with some residual power in the circular polarization at that same frequency (Stokes V). The degree of circular polarization (Stokes V/I) is quite small, again centered near 75 MHz. However, the residual circular polarization and degree of circular polarization shown may be due to polarization leakage at the antenna. Measurements of future radio bursts may reveal more definite information.
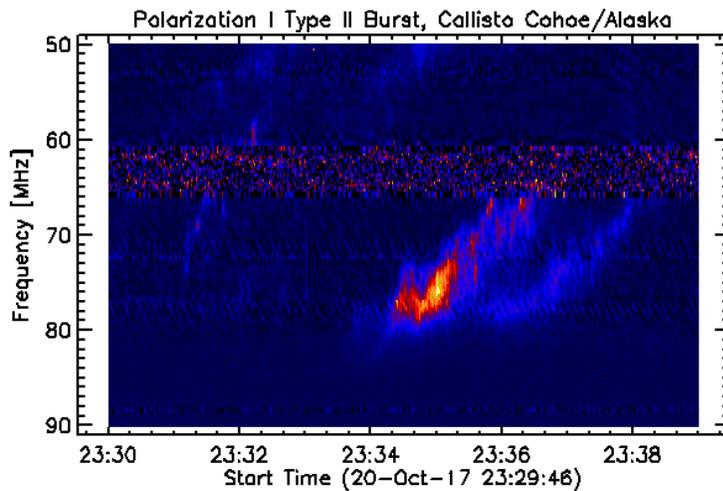

Figure 19 ~ Cohoe, Alaska USA: Dynamic spectrum showing total power (summation), LHCP + RHCP, or Stokes I parameter. I was not able to sufficiently suppress the interference between about 60 and 65 MHz in this and the next polarization images. Also, I found it futile to attempt the same background subtraction and color map in the three polarization images.
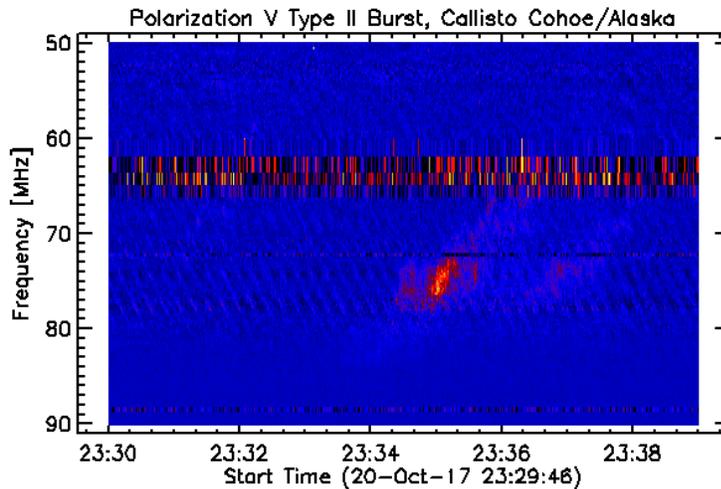
Figure 20 ~ <u>Cohoe, Alaska USA</u>: Dynamic spectrum showing net circular polarization (difference), |LHCP − RHCP|, or Stokes V parameter. Some residual circular polarization is indicated in the 2nd harmonic near 75 MHz, but this could be due to polarization leakage at the antenna. The band between 60 and 65 MHz and the tilted streaks are interference.
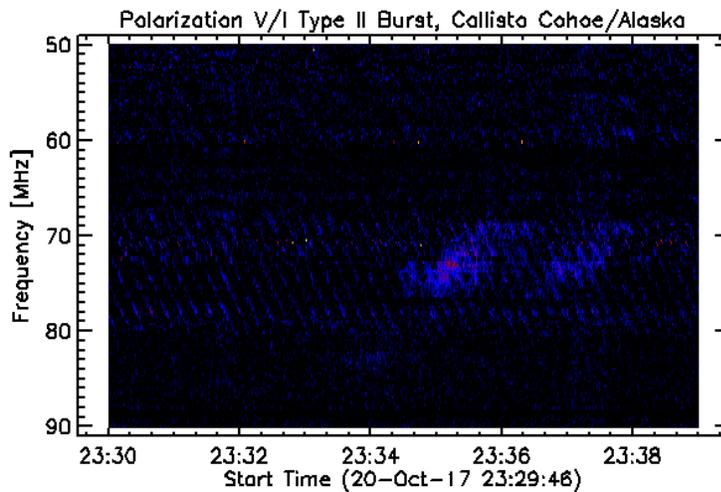

Figure 21 ~ <u>Cohoe, Alaska USA</u>: Dynamic spectrum showing degree of polarization, d_C, or Stokes V/I. The degree of polarization in the 2nd harmonic near 75 MHz is quite small. The tilted streaks are interference.

5. Conclusions

Type II solar radio bursts are described in this paper with emphasis on and analysis of a burst received 20 October 2017 at Cohoe Radio Observatory in Alaska. Type II radio bursts are one part of a more extensive solar eruption event, which includes a flare and a coronal mass ejection. The Type II frequency drift rate can be used to infer the speed of the CME, which is a useful parameter in space weather predictions. If the burst has split-bands, it also may be used to estimate the coronal magnetic field.

Graphical methods and a simple solar corona model are applied to the 20 October burst to derive estimates of the CME shock speed and solar magnetic field. The CME speeds calculated using these methods are comparable to graphical analysis of imagery from the STEREO A spacecraft coronagraph. The results from the magnetic field analysis are in line with measurements of large numbers of Type II radio bursts by professional investigators.

The polarization characteristics of the Type II radio burst also are analyzed and indicate a largely unpolarized emission except in the 2nd harmonic near 75 MHz, but this could be due to polarization leakage at the antenna.

6. References and Web Links

[Cho07]   Cho, K., Lee, J., Gary, D., Moon, Y. and Park, Y., *Magnetic Field Strength in the Solar Corona from Type II Band Splitting*, Astrophysical Journal, 665, pp. 799-804, 2007 (available at: http://adsabs.harvard.edu/abs/2007ApJ...665..799C)

[Choudhuri]   Choudhuri, A., Astrophysics for Physicists, Cambridge University Press, 2010

[Dulk]   Dulk, G., *Radio Emission from the Sun and Stars*, Annual Review of Astronomy and Astrophysics, 1985, 23, 169-224 (available at: http://planeterrella.osug.fr/IMG/pdf/stellar_emissions.pdf)

[Hariharan15] Hariharan, K., Ramesh, R., and Kathiravan, C., *Observations of Near-Simultaneous Split-Band Solar Type-II Radio Bursts at Low Frequencies*, Solar Physics, 2015, 290:2479–2489, DOI 10.1007/s11207-015-0761-5 (available at: https://www.researchgate.net/publication/283154669_Observations_of_Near-Simultaneous_Split-Band_Solar_Type-II_Radio_Bursts_at_Low_Frequencies)

[Kraus]   Kraus, J., Radio Astronomy, 2nd Ed., Cygnus-Quasar Books, 1986

[Kundu]   Kundu, M., Solar Radio Astronomy, John Wiley, 1965

[Marr]   Marr, J., Snell, R. and Kurtz, S., Fundamentals of Radio Astronomy – Observational Methods, CRC Press, 2016

[Monstein12]   Monstein, C., *Estimation of CME Shock Wave Speed Out of Type II Solar Bursts*, Society of Amateur Radio Astronomers, *Radio Astronomy*, pg 38-44, September-October 2012

[Newkirk61]   Newkirk, G., *The Solar Corona in Active Regions and the Thermal Origin of the Slowly Varying Component of Solar Radio Radiation*, Astrophysical Journal, Vol. 133, p.983, 1961 (available at: http://adsabs.harvard.edu/full/1961ApJ...133..983N)

[Smerd75]   Smerd, S., Sheridan, K. and Stewart, R., *Split-Band Structure of Type II Radio Bursts from the Sun*, Astrophysical Letters, Vol. 16, pp. 23-28, 1975 (available at: http://adsbit.harvard.edu/full/seri/ApL../0016//0000028.000.html)

{ALERT}   http://services.swpc.noaa.gov/products/alerts.json
{Callisto} http://www.e-callisto.org/
{EVENT}   ftp://ftp.swpc.noaa.gov/pub/indices/events/20171021events.txt
{FRCST}   ftp://ftp.swpc.noaa.gov/pub/forecasts/discussion/10211230forecast_discussion.txt
{NASA}   https://sdo.gsfc.nasa.gov/assets/img/browse/2017/10/20/20171020_232942_512_0304.jpg
{RAPPV}   http://www.e-callisto.org/Software/RAPPViewer.jar
{STEREO}   https://stereo-ssc.nascom.nasa.gov/cgi-bin/images

7. Acknowledgement

The instrumentation at Cohoe Radio Observatory is briefly described along with an RF system block diagram (figure A-1) and few pictures of the instrumentation (figure A-2). A dual Callisto installation is connected to a Long Wavelength Array (LWA) antenna, one instrument for each polarization. The Callisto has a native frequency range of 45 to 870 MHz and 62.5 kHz frequency resolution. The frequency range is reduced to 45 to 93 MHz for compatibility with the antenna. It is setup for 192 usable channels with 250 kHz spacing as determined by a frequency configuration file in the Callisto software. When in operation, each Callisto consumes about 2.8 W at 12 Vdc.
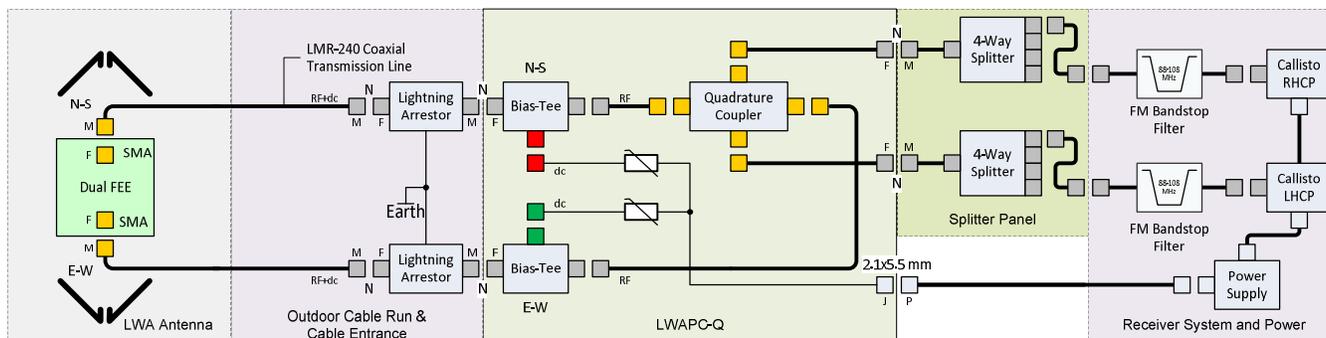

Figure A-1 ~ RF system block diagram. The major blocks are, left-to-right, the LWA antenna, coaxial cable transmission lines and cable entrance facility with lightning arrestors, LWA Power Coupler, 4-way Splitter Panel, Callisto instruments and associated power supplies.

The antenna is a crossed-dipole with sloping elements with a frequency range of 5 to 100 MHz. Front-end electronics (FEE) consisting of dual low noises amplifiers (LNA) are installed at the junction of the elements, making the LWA antenna an active antenna. Each LNA in the FEE consumes approximately 3.5 W at 15 Vdc and provides 35 dB gain and 2.9 dB noise figure. Antenna power is provided by an LWA Power Coupler with quadrature coupler (LWAPC-Q). The LWAPV-Q includes two bias-tee modules, power input filtering an overcurrent protection. The quadrature coupler provides right-hand and left-hand circular polarizations (RHCP and LHCP, respectively) from the two linearly polarized dipoles. The RHCP and LHCP outputs from the LWAPC-Q are connected to 4-way RF splitters that allow connection of multiple receivers. Unused splitter ports are resistively terminated.

The Callisto instruments are controlled by small desktop PC running Windows 10 operating system. Two instances of the *Callisto* application software are run to control and collect data as determined by a scheduler configuration file. The scheduler file is setup to observe only during daylight hours and is updated every other month. The FITS data files are transferred to the FHNW e-Callisto server in Switzerland. Data upload uses the File Transfer Protocol (FTP) driven by a *Perl* script. The Perl script is under control of the *System Scheduler* software application program that invokes the script at 15 minute intervals, corresponding to the FITS data intervals used by the Callistos. The PC uses the *Startup Delayer* software application to automatically load the Callisto software at PC startup.

Ancillary equipment includes a multi-voltage power supply system (5, 12, 15, 24 and 16 Vdc), uninterruptible power system (UPS) for the PC, web-controlled relay system and an industrial cellular modem for internet

access. The UPS is monitored by the *Power Panel* software application supplied with it. The *TeamViewer* software application is used to access the observatory from Anchorage. Cellular service is provided by AT&T 4G LTE service. A diversity antenna system at 18 m above ground level is used with the cellular modem to ensure adequate connection in the forested area where CRO is located. A *Web Power Switch* provides remote controlled relays for rebooting the Callistos and for controlling other power equipment in the observatory.

Figure A-2 ~Upper-left: Callisto instrument. Power connections and control are on the opposite panel (not shown); Upper-right: LWA Antenna with a protective fence to prevent damage by rampaging moose that frequent the area. The antenna is about 1.5 m high; Lower-left: LWA Power Coupler – Quadrature (LWAPC-Q). Additional RF connections are on the opposite panel (not shown).

Author: Whitham Reeve is a contributing editor for the SARA journal, Radio Astronomy. He obtained B.S. and M.S. degrees in Electrical Engineering at University of Alaska Fairbanks, USA. He worked as an engineer and engineering firm owner/operator in the airline and telecommunications industries for more than 40 years and now manufactures electronic equipment for use in radio astronomy. He has lived in Anchorage, Alaska his entire life. Email contact: whitreeve(at)gmail.com

Document information

Author: Whitham D. Reeve
Copyright: © 2018 W. Reeve
Revisions: 0.0 (Draft started 22 Oct 2017)
             0.1 (Added citations, calculations and images, 05 Nov 2017)
             0.2 (Added polarization and software tool images, 07 Nov 2017)
             0.3 (Completed 1st draft, 09 Nov 2017)
             0.4 (Added STEREO image analyses, 14 Nov 2017)
             0.5 (Completed STEREO image analysis, 18 Nov 2017)
             0.6 (Added summary table of speed measurements, 08 Jan 2018)
             0.7 (Added Appendix, 14 Jan 2018)
             0.8 (Revised Type II scenario, 25 Jan 2018)
             0.9 (Revised Type II scenario again, 17 Feb 2018)

Word count: 7862
File size: 20415532